



**Optical Spectroscopic Study on Two-Dimensional Group-VI  
Transition Metal Dichalcogenides**

Journal:	<i>Chemical Society Reviews</i>
Manuscript ID:	CS-TRV-07-2014-000265.R2
Article Type:	Tutorial Review
Date Submitted by the Author:	05-Apr-2015
Complete List of Authors:	Zeng, Hualing; Chinese University of Hong Kong, Physics Cui, Xiaodong; The University of Hong Kong, Physics

# Optical Spectroscopic study on two-dimensional group-VI Transition Metal Dichalcogenides

Hualing Zeng<sup>1</sup> and Xiaodong Cui<sup>2</sup>

1. Department of Physics, The Chinese University of Hong Kong, Hong Kong, China

2. Physics Department, The University of Hong Kong, Hong Kong, China

Keywords: transition metal dichalcogenides, monolayers, spin-valley coupling, spintronics, valleytronics

## ***Key Learning Points:***

1. An overview of recent significant advances in optical experiments on 2D group-VI TMDs.
2. Optical properties of monolayer group-VI TMDs as direct band-gap semiconductors.
3. Optical characterization techniques of 2D TMDs.
4. Excitonic effect in 2D semiconductors.
5. Optical study of valley, spin, and layer degrees of freedom in 2D TMDs.

**Abstract:** The ultimate goal of making atomically thin electronic devices stimulates intensive research in layered materials, in particular the group-VI transition metal dichalcogenides (TMDs). Atomically thin group-VI TMD crystals with 2H stacking order emerging as a family of intrinsic 2-dimensional (2D) semiconductors with a sizeable bandgap in the visible and near infrared range, satisfy numerous requirements for ultimate electronics and optoelectronics. In addition, the characteristic inversion symmetry breaking presented in monolayer TMDs leads to non-zero but contrasting Berry curvatures and orbit magnetic moments at  $K/K'$  valleys located at the corners of the first Brillouin zone. These features provide an opportunity to manipulate electrons' additional internal degrees of freedom, namely the valley degree of freedom, making monolayer TMDs a promising candidate for the conceptual valleytronics. Besides, the strong spin-orbit interactions and the subsequent spin-valley coupling demonstrated in

atomically thin group-VI TMDs open potential routes towards quantum manipulation. In this tutorial review, we highlight recent advances in optical study on electronic structures, vibrational properties, excitonic effects, valley dependent optical selection rules, and the interplay of valley, spin, and layer degrees of freedoms in this class of atomic 2D semiconductors including MoS<sub>2</sub>, MoSe<sub>2</sub>, WS<sub>2</sub>, and WSe<sub>2</sub>.

### ***1. Introduction.***

Novel properties often emerge as the dimensionality of materials is reduced. One example is the behavior of the massless Dirac Fermion displayed in graphene, a truly two-dimensional material with only one layer of carbon atoms that can be exfoliated from bulk graphite.<sup>1,2</sup> Pristine graphene is a semi-metal with linear band dispersion in the low-energy electronic structure showing ultra-high ambipolar carrier mobility. However, this gapless character limits graphene's application in electronics as the lack of a bandgap fails to provide an "off" state for a logic transistor which is the building block of modern electronics. The success and the limitation of graphene ignite the research in exploring other 2D atomic crystals, which is not only for the goal of ultimate electronics but also for elegant scientific aspects in the field of physics, chemistry, material science, and biology. Group-VI transition metal dichalcogenides (TMDs), a class of van der Waals stacked crystals with generalized formula MX<sub>2</sub> (M=Mo,W; X=S,Se), are among the top-notch candidates. The TMDs with 2H stacking order, which is the most stable phase and the focus of all the interests at this stage, display semiconducting behavior with suitable energy bandgap in the visible and near infrared range. Analogous to graphite, TMDs can be thinned to

ambient-stable monolayers via mechanical exfoliation or chemical synthesis, presenting remarkable physical and chemical properties which are of great potential for applications in optoelectronics, catalysis, sensors, spintronics, and valleytronics.<sup>3-10</sup>

The study on the family of  $\text{MX}_2$  thin films started as early as in 1960s, while the focus was only devoted to material characterization. Equipped with the pioneering experiences in graphene, Geim's group first reported the observation of macroscopic monolayer  $\text{MoS}_2$ .<sup>11</sup> Their semiconducting nature was initially revealed by electrical conductivity measurements, suggesting a sizeable band-gap of energy more than 0.6eV. Following the fast growing interests in 2D atomic crystals, several years after, two independent groups reported the experimental evidence of the transition from indirect energy gap at bulk form to direct band-gap at monolayer  $\text{MoS}_2$  via photoluminescence (PL) spectroscopy.<sup>3,4</sup> The next milestone of the 2D TMD research was the demonstration of a monolayer  $\text{MoS}_2$  field effect transistor with high current on/off ratio and decent electron mobility more than  $200\text{cm}^2\text{v}^{-1}\text{s}^{-1}$  at room temperature.<sup>5</sup> These breakthroughs have greatly stimulated chemists and material scientists to develop new methods to produce ultrathin TMD films in a controllable way, including the chemical vapor deposition (CVD)<sup>12</sup> and liquid exfoliation.<sup>13</sup>

Meanwhile, the need for noninvasive and accurate material characterizations encouraged the study on vibrational properties<sup>14-19</sup> and the nonlinear optics<sup>15, 20-22</sup>. Very recently, significant interests rise in attempting to manipulate the spin and valley degrees of freedom in group-VI 2H TMDs owing to the inversion symmetry breaking

and the strong spin-orbit coupling (SOC) in monolayer TMDs, i.e. the optical valley control,<sup>6-9</sup> valley coherence,<sup>23</sup> and valley Hall effect<sup>24</sup>. The strong coupling of the spin and valley degrees of freedom in group-VI 2H TMDs makes them promising candidates for applications in valley based electronics, or so called valleytronics,<sup>15, 25-28</sup> which utilizes the electron's valley degrees of freedom as an information carrier, in analogous to spintronics that exploits electron spin.

Motivated by the rapid progresses in the field of layered TMD research, this review focuses on the emerging optical properties of 2H-MX<sub>2</sub>. For the sake of simplicity, if not specially mentioned, the crystal structure of the group-VI TMD thin films is in a form of 2H phase. In this review we highlight recent advances of optical spectroscopic study on this class of emerging 2D semiconductors, mainly on MoS<sub>2</sub>, MoSe<sub>2</sub>, WS<sub>2</sub>, and WSe<sub>2</sub>. We review the experimental progresses related to the electronic structure, characteristic vibrational modes, structure symmetry and the effect of electron-electron interactions in atomically thin TMD films. We put an emphasis on the unprecedented spin-valley related optical phenomena in both monolayer and multilayer TMDs. In the end, we outlook the challenges and future developments in 2D TMD research.

## ***2. Fundamental optical properties***

The family of group-VI TMDs share a similar structure of X-M-X covalently bonded hexagonal quasi-2D network weakly stacked by van der Waals forces usually with Bernal stacking order (2H). A single layer MX<sub>2</sub> (1H) has a prismatic unit cell where the metal atom sits in the center of a trigonal prismatic coordination, being bound to

six chalcogen atoms with strong covalent bonds as shown in Figure 1a. These trigonal prisms are interconnected through the bonds between the chalcogen and metal atoms in the trigonal bipyramidal configuration with  $D_{3h}^1$  crystal symmetry. The inversion symmetry is explicitly broken at single layer since within each slab the chalcogen atoms will be mapped into empty positions if taking the metal atom as the inversion center. Nevertheless, this spatial inversion symmetry is restored in their bulk form as the weakly van der Waals coupled layers follow the  $2H$  stacking order, in which any two adjacent layers are 180 degree in plane rotation of each other (Figure 1b). The metal atoms of a given layer are sitting exactly on top of the chalcogen atoms of its neighboring layer, which is well represented by  $D_{6h}^4$  space group. The same lattice structure of the materials in TMDs family naturally brings the essentially similar physical properties, including the electronic band structure, the phonon modes, and the structure symmetry.

As van der Waals packed layered materials, ultrathin TMDs can be prepared by mechanical exfoliation from bulk single crystals. This method was initially developed in the discovery of graphene. Tremendous efforts on the direct large-scale synthesis via Chemical vapor deposition (CVD)<sup>12</sup> and liquid exfoliation<sup>13</sup> have been making promising progresses. Compared to natural  $2H$   $MX_2$  crystals, the synthetic or chemically exfoliated ultra-thin films could exist in variety of crystalline phases, including  $1T$ ,  $2H$  and  $3R$  etc, presenting distinct electronic structures, for example the  $1T$  phase, which is proved to be metallic.<sup>29</sup> The structure change from  $1T$  phase to  $2H$  phase can be achieved by low temperature annealing.<sup>29</sup>

Identifying 2D TMD is readily realized with regular bright field optical microscopes. Monolayer and multilayer TMDs on dielectric capped substrates can be visualized under an optical microscope due to the color contrast, which offers the most efficient way for thickness screening. Quantitative optical characterization on film thickness could be provided with Raman, photoluminescence and second harmonic generation spectroscopy, which all will be addressed in this tutorial. Further characterization can be achieved by various means such as scanning probe microscopy and transmission electron microscopy.

### ***2.1 Electronic properties***

Recent theoretical calculations show that the low-energy electronic states are strongly dependent on crystal thickness in atomically thin  $\text{MX}_2$  films.<sup>30</sup> There exists a crossover from an indirect-gap semiconductor at multilayers to a direct-band-gap one at the limit of monolayers.<sup>3, 4, 15, 31</sup> For bulk and multilayer TMDs, the conduction band minimum (CBM) is located at the middle point between the high symmetric K and  $\Gamma$  points in the Brillouin zone, while the valence band maximum (VBM) pins at  $\Gamma$  point, leading to an indirect band-gap. As the bulk thins to monolayers, both the CBM and VBM shift to K point due to quantum confinement effect in 2D system, which yields a direct-gap semiconductor for monolayer TMDs. The intriguing evolution of the electronic band structure presented in ultra-thin  $\text{MX}_2$  films results from different origins of the electronic states at K and  $\Gamma$  points.<sup>4, 6, 30</sup> The conduction and valence bands near K points come from the hybridization of the d-electron orbits of the metal atoms, which are localized and show insensitive against interlayer hopping since the

metal atoms are located in the middle layer of the X-M-X sandwich. Comparatively, the states near  $\Gamma$  point carry the characteristics of the anti-bonding p-orbits of chalcogen atoms. They are affected strongly by the interlayer coupling and their energies depend sensitively on their thickness. Atomically thin TMD films, including monolayers and multilayers, present an emergent class of 2D semiconductors that can be widely recognized as a platform for ultimate electronics. Especially at the monolayer limit, the sizeable direct band-gap in visible and near infrared range makes them ideal candidates for optoelectronic applications.

As the electronic properties for the family of group-VI TMDs are similar, herein we take  $\text{MoS}_2$  and  $\text{WS}_2$  as typical examples. Figure 2a and 2d show the calculated electronic structures of monolayer, bilayer and bulk  $\text{MoS}_2$  and  $\text{WS}_2$  by first principle simulations respectively.<sup>32</sup> The band-gaps of both  $\text{MoS}_2$  and  $\text{WS}_2$  nanosheets show a dramatic thickness dependence. It shifts from 1.2eV (1.3eV) at bulk form to 1.9eV (2.1eV) in the monolayer limit for  $\text{MoS}_2$  ( $\text{WS}_2$ ). Accompanying the increase of the band-gap with the decreased layer thickness, they come across a transition from indirect band-gap materials to direct-gap semiconductors as both the CBM and VBM shift to K points at monolayers due to the quantum confinement effect. This change in electronic properties can be monitored by the energy evolution of the absorption/reflection spectra and the band-edge emissions in the PL measurements.<sup>3, 4, 15, 31</sup> Besides, the strong evidence of the direct band-gap at monolayers lies in that the PL intensity (quantum efficiency) of monolayers is several orders of magnitude higher than that of the bulk counterparts, as the involvement of phonon- or defect-scatterings

for satisfying the momentum conservation in optical transitions is waived in direct-gap semiconductors. The PL quantum yield of monolayers was found to be  $10^4$  fold of that in bulk, which is consistent with the characteristic of a direct-gap semiconductor. Representative observations on MoS<sub>2</sub> and WS<sub>2</sub> are shown in Figure 2. This makes monolayer TMDs ideal candidates for optical emitters, photovoltaic cells, and optoelectronic devices.

As ultrathin TMDs are 2D atomic crystal presenting ultimate surface-to-volume ratio, all chemical bonds are exposed as surface states which are sensitive to environment perturbations. Consequently surface modifications in 2D TMDs play a much more pronounced role in modifying their electronic properties than in their bulk counterparts.<sup>10</sup> Recent experiments clearly demonstrated that the electronic structure and optoelectronic properties of monolayer TMDs can be significantly yet selectively tuned by chemical functionalization with some functional groups.<sup>33, 34</sup> The high sensitivity and reasonable selectivity of the electronic and optoelectronic properties to chemical modifications stimulates growing interests in potential applications of chemical and biological sensing and catalysis.

Another distinct feature of atomically thin TMD films is the giant Zeeman-like spin-orbit coupling (SOC) originating from the heavy metal d-orbits. For monolayer TMDs, both the conduction and valence band edges located at K points are constructed by heavy metal d-orbits  $d_{z^2}$  and the mix of  $d_{x^2+y^2}$  and  $d_{xy}$  respectively. Band structure calculations show that the SOC splits the valence band into two at the top (K points) while the degeneracy of conduction band remains,

which can be seen from the band structure of monolayer MoSe<sub>2</sub> as shown in Figure 3a.<sup>6, 35, 36</sup> The magnitudes of the valence band splitting are predicted to be from 160meV to 460meV, which equals to the Zeeman splitting strength for electrons in a magnetic field up to 10<sup>2</sup> and even 10<sup>3</sup> tesla. The split valence bands at K points give rise to two direct interband optical transitions, namely the A and B excitonic transitions. By monitoring the energy difference between A and B transitions in optical spectra, for instance the absorption spectrum, the differential transmittance/reflectance measurements, or the PL spectra, the splitting strength can be directly determined as demonstrated in Figure 3b.<sup>36</sup> The values of the SOC induced valence band splitting are found to be around 0.15eV and 0.2eV for MoS<sub>2</sub> and MoSe<sub>2</sub> respectively,<sup>3, 4, 36</sup> while are greatly enhanced in tungsten dichalcogenides with the value of around 0.4eV for both.<sup>15, 31</sup> The giant SOC in ultrathin TMDs layers benefits them in potential applications in spintronics.

To give a clear summary for the fundamental optical properties of 2D TMDs, we make a table listing the transition energies for the A and B excitons and the SOC strength in all four monolayer TMDs.

Table1. Summary of the electronic properties of 2D TMDs

	A (eV)	B (eV)	SOC (2λ)
MoS <sub>2</sub>	1.88 in Ref. 3	2.03 in Ref. 3	150meV
MoSe <sub>2</sub>	1.67 in Ref. 37 at 20K	1.87 in Ref. 37 at 20K	200meV
WS <sub>2</sub>	1.94 in Ref. 16	2.33 in Ref. 16	390meV
WSe <sub>2</sub>	1.65 in Ref. 16	2.05 in Ref. 16	400meV

## 2.2 Vibrational properties

Raman and infrared (IR) spectroscopy are the major techniques to evaluate the vibrational modes. Given the tiny size (usually tens of microns) of the current exfoliated 2D TMD crystals, however, the IR study is rarely reported partially due to the limit of spatial resolution and low cross section. Raman spectroscopy has been proven to be an accurate and noninvasive technique of thickness characterization as well as a versatile method to study the phonon modes in 2D materials.<sup>14, 16</sup> Intensive research efforts focus on four characteristic Raman-active modes of TMD crystals,<sup>14-19</sup> namely the  $A_{1g}$ ,  $E_{2g}^1$ ,  $E_{2g}^2$ , and  $B_{2g}^2$  modes. These optically active phonons can be divided into two groups as shown in Figure 4a.  $A_{1g}$  and  $E_{2g}^1$  modes originate from the optical vibrations of the metal and chalcogenide atoms within the same slab, while the latter two modes are from the rigid motion of the whole layer relative to each other. The thickness monitoring technique with the Raman scattering spectroscopy on TMD multilayers was firstly demonstrated by Lee et al.<sup>14</sup> in MoS<sub>2</sub> thin films, where the energy difference  $\Delta\omega$  of the out-of-plane vibrational  $A_{1g}$  mode and the in-plane vibrational  $E_{2g}^1$  mode was used as a film thickness indicator. For monolayer MoS<sub>2</sub>  $\Delta\omega$  is around 19cm<sup>-1</sup> while its value increases to 21cm<sup>-1</sup> in bilayer MoS<sub>2</sub>, showing a strong thickness dependence which can be clearly seen in Figure 4b and 4c. Similar layer thickness dependence of  $A_{1g}$  and  $E_{2g}^1$  modes in WX<sub>2</sub> has been observed but with much less significance.<sup>15, 19</sup> It is because the heavier tungsten atom makes the eigen-vibrational frequency less sensitive to the environmental changes. Nevertheless, among their Raman active phonon modes the

$E_{2g}^2$  and  $B_{2g}^2$  vibrational modes are generic for layered crystal structure and can be regarded as collective interlayer phonon modes. As sketched in the lower panel of Figure 4a, the  $E_{2g}^2$  mode or so called shear mode is the rigid oscillation of adjacent layers in the layer plane direction, while  $B_{2g}^2$  mode or so called “layer breathing mode (LBM) or compression mode” is the rigidly oscillating motions of layers vertical to the layer plan. It is worth nothing that the  $B_{2g}^2$  mode is Raman inactive for bulk TMDs and turns to Raman active at ultra-thin multilayers owing to the translation symmetry breaking along the c-axis.<sup>19</sup> Despite of rich information carried in the interlayer phonon modes of 2D TMDs, experimental studies on  $E_{2g}^2$  and  $B_{2g}^2$  modes have been rarely reported owing to technique challenging. The difficulty lies in that the interlayer phonons are usually of very low energy ( $<50\text{cm}^{-1}$ ) and therefore are hard to be distinguished from the Rayleigh background scattering with regular commercial Raman spectrometers. It is not until the applications of multi-stage spectrometer or volume-Bragg-grating (VBG) filters with ultra-narrow spectral band-width in Raman scattering measurements that these low energy phonons in layered TMDs can be directly detected.<sup>16-19</sup> The two low-frequency Raman modes show contrasting thickness dependences as illustrated in Figure 4d and 4e with multilayer MoS<sub>2</sub> as an example.<sup>16</sup> The frequency of shear mode  $E_{2g}^2$  shows a significant increase with the increase of the film thickness. In contrast, the frequency of layer breathing mode decreases with the increase of film thickness and totally fades in bulks.<sup>16</sup> The observed opposite evolution of the two low-frequency interlayer phonon modes provides a more precise thickness measurement for 2D TMDs, for

instance, up to 19 layers for multilayer MoS<sub>2</sub>.<sup>18</sup> Besides, the study on shear mode and layer breathing mode gives valuable information on the interlayer interactions and their mechanical properties, for example the interlayer frictional force constant and the shear modulus, which were thought to be done impossibly in optical way.

### ***2.3 Second harmonic generation in 2D TMD thin sheets***

The structure symmetry of materials plays an important role in light-matter interactions. For monolayer and odd-numbered TMD ultrathin films with *2H* packing order they are non-centrosymmetric as the inversion symmetry is explicitly broken and are classified as  $D_{3h}^1$  space group. Nevertheless, the spatial inversion symmetry is restored in even-layer TMD crystals with *2H* packing order. To probe the structural inversion symmetry of materials, an elegant tool is the second harmonic generation (SHG) in which the nonlinear optical process combines two input photons to one photon with twice the energy. A simple classical model indicates that the efficiency of SHG is determined by the 2<sup>nd</sup> order susceptibility  $\chi^2$  of the materials. By applying a simple symmetry analysis, it is easy to conclude that  $\chi^2$  must be zero for crystals with inversion symmetry as the spatial reversal transformation  $r \rightarrow -r$  makes  $\vec{P}(\omega, r) = -\vec{P}(\omega, -r)$ , where the light induced material's polarization could be described in a classical way as  $\vec{P}(\omega, r) = \epsilon_0(\chi^1 \vec{E}(\omega, r) + \chi^2 \vec{E}(\omega, r) \cdot \vec{E}(\omega, r) + \dots)$ . In contrary, significant SHG implies inversion symmetry breaking. Thereby, SHG can be used as a sensitive probe to the inversion symmetry of materials and the experimental evidences have been demonstrated in atomically thin TMD crystals by independent groups.<sup>15, 20-22</sup> The efficiency of SHG from 2D TMDs displays an

even-odd oscillation with a decay envelop as shown in Figure 5 where monolayer and multilayer WS<sub>2</sub> are taken as an example.<sup>15</sup> The strongest SHG comes from monolayer TMDs and intense SHG is observed on odd-numbered layers only, as illustrated in Figure 5c. The dramatic even-odd oscillation pattern of the SHG from 2D TMDs is the direct evidence for the variation of structure inversion symmetry (Figure 5d), which is in consistence with the presentence (absence) of spatial inversion symmetry in even-layers (odd-layers). The layer number dependent SHG in ultrathin TMD films provides a fast and in-situ layer characterization method and confirms the Bernal stacking order (2H) in multilayer TMDs.<sup>15</sup>

Further polarization resolved SHG experiments demonstrate that the SHG microscopy of monolayer TMDs is able to detect the atomic edge and grain boundaries and determine the orientations of 2D crystal domains,<sup>20-22</sup> which are thought to be carried out only under the help of the atomic-resolution scanning probe microscopes or transmission electron microscopes. This amazing ability arises from the monolayer TMDs' spatial symmetry. For monolayer TMDs, the symmetry is represented by  $D_{3h}^1$  space group, resulting in three-fold rotational symmetry of the crystallographic orientation with respect to the c-axis. When the excitation photon in SHG experiments is linearly polarized and chosen to be in a normal incidence configuration ( $z\bar{z}$ ), the responses of the two orthogonal components of second harmonic field from monolayers,  $P_x$  and  $P_y$ , follow  $\sin 3\theta$  and  $\cos 3\theta$  dependence respectively, where  $\theta$  is the angle between the orientation of incident polarization and the zigzag in-plane direction in monolayer TMDs along which the mirror

symmetry holds. The polarization resolved SHG signal  $I_x$  or  $I_y$  is thus proportional to  $\sin^2 3\theta$  or  $\cos^2 3\theta$ , showing a strong dependence on crystal orientation.<sup>20, 21</sup> The sensitivity of the linearly polarized SHG intensity with respect to lattice direction makes it possible to identify the 2D crystal domains and grain boundaries via all-optical way, and the technique has been demonstrated in large CVD-grown polycrystalline monolayer TMD as shown in the lower panel of Figure 5.<sup>22</sup>

#### ***2.4 Excitonic effect in 2D TMDs thin sheets***

Bulk TMD crystals displays an excitonic feature in their optical properties owing to the van der Waals layered structure and the heavy effective mass of valence/conduction bands. The binding energy of exciton, a kind of quasi-particles composed of tightly bounded electron-hole pairs, ranges from 50 to 80meV (vs. the thermal energy 26meV at room temperature ~300K) in bulk TMD crystals. In a single-particle picture, optical absorption occurs when an electron is excited from valence band to conduction band by absorbing a photon with energy no less than the electronic band gap, and photoluminescence is just a reverse process but dominated by the band-edge emission, an optical transition from the CBM to the VBM. The optical transitions are directly related to the electronic band gap. In an excitonic picture, attractive Coulomb interactions between photon-generated electrons and holes bond the electron-hole pairs to excitons, and consequently reduce the threshold of the optical interband transition by the binding energy of excitons. If the binding energy is significant compared with the environmental perturbations (i.e. temperature), optical properties would have pronounced excitonic features. Coulomb interactions

are dramatically enhanced in 2D crystals compared with the conventional semiconductors owing to the spatial confinement and the reduced dielectric screening which is particular for excitons with in-plane orientation.<sup>37</sup> A direct consequence of strong Coulomb interactions is the giant excitonic features dominating the optical properties. The band-edge emissions and the pronounced absorption peaks of 2D TMD crystals (not only monolayers, but also multilayers) are attributed to excitonic transitions, instead of direct band-to-band transitions. Calculations with various methods of density function theory (DFT) suggest the exciton binding energy of monolayer TMDs ranging from 0.6 to 1.1eV which is a significant fraction of the corresponding band-gap.

Early experimental evidence for the excitonic nature of the optical transitions in monolayer TMDs comes from the observation of the electron-bounded excitons, so called trions in the PL and absorption spectra of monolayer MoS<sub>2</sub><sup>38</sup> and MoSe<sub>2</sub><sup>36</sup>. The binding energy of the trions in monolayer TMDs (~20meV in MoS<sub>2</sub>, ~30meV MoSe<sub>2</sub>, 35meV in WS<sub>2</sub>, and 24-40meV in WSe<sub>2</sub>) is about one order of magnitude larger than that in conventional materials and it makes the trion state easily visible in PL and absorption spectra even at room temperature as displayed in Figure 6. It implies strong Coulomb interactions and subsequently the giant exciton binding energy in monolayer TMDs.

Conventionally the exciton binding energy is extracted by the energy difference between the ground-state exciton and the onset of the direct band-to-band transition (single particle gap) in the absorption spectrum. In monolayer TMDs, however, the

strong electron-phonon coupling and the energy overlap with higher energy bands smear the discrete excitonic states and the onset of the direct band-to-band transition in the absorption spectrum. There are two routes towards measuring the exciton binding energy of monolayer TMDs. One is through optical absorption spectroscopy at cryogenic temperature at which the electron-phonon coupling is suppressed. Chernikov *et. al.*<sup>39</sup> observed series of s-type excited states of band-edge excitons of monolayer WS<sub>2</sub> at 4K. The exciton binding energy of 0.39eV was extracted with a modified 2D hydrogen Rydberg model. The other approach is through two-photon photoluminescence excitation spectroscopy (TP-PLE) in which the intensity of the band-edge exciton emission is monitored as a function of two-photon absorption, each photon with energy below the band gap. Two-photon absorption could be described as a third order nonlinear process involving simultaneous absorption of two photons and may follow the different optical selection rules from the linear (one-photon) process. For an intrinsic 2D system, the two-photon absorption is associated with p-type excitons while the one-photon (linear) process is with s-type excitons.<sup>40</sup> Here s- and p-type are the characteristic labels for exciton envelop functions describing the exciton states in a similar way as atomic orbitals. The bright excitons in one-photon process, for example the high-energy exciton states, are usually dark in two-photon process; whereas direct band-to band transitions survive in both one-photon and two-photon processes. Consequently the high-energy exciton states around  $\Gamma$  points which may overlap with the onset of band-to-band transition are inactive in two-photon absorption. As the s-type and p-type excitons have different spatial

wavefunctions and lifetime, besides, they may have different strength of exciton-phonon coupling. So the two processes (one-photon and two-photon) probe complementary information. TP-PLE experiments reveal discrete p-type excited states of band-edge excitons and/or the single particle gap.<sup>41-44</sup> The exciton binding energy is extracted by the energy difference between the optical gap and the single particle gap. Although there exists quantitative discrepancy among the present experimental findings as listed in table 2, a strong excitonic feature at monolayer TMDs is the consensus. The strong excitonic effect suggests unprecedented strong exchange interactions and many-body interactions in monolayer TMDs.

Table 2. Summary of the exciton binding energies of monolayer TMDs.

Monolayer TMDs	Theory (eV)	Experimental (eV)
MoS <sub>2</sub>	1.1 <sup>45</sup> , 1.03 <sup>46</sup>	0.57 <sup>47</sup>
MoSe <sub>2</sub>	0.78 <sup>45</sup> , 0.91 <sup>46</sup>	0.55 <sup>42</sup>
WS <sub>2</sub>	1.04 <sup>46</sup>	0.7 <sup>43,44</sup> , 0.32 <sup>39</sup>
WSe <sub>2</sub>	0.90 <sup>46</sup>	0.6 <sup>48</sup> , 0.37 <sup>41</sup>

### ***3. Spin and valley physics in 2D TMDs***

#### ***3.1 valley polarization in monolayer TMDs via optical pumping***

Most conventional electronic devices utilize the electric charge of electrons to perform functions. Unexhausted efforts have been devoted to explore novel electronic technology that exploits other internal degrees of freedom of electrons in addition to electric charge. One representative example is spintronics in which electron spin acts as information carriers. In addition to spin, there exists valley degree of freedom in TMD crystals owing to their hexagonal lattice structures. TMD crystals with buckled

hexagonal lattice have degenerate but inequivalent K and K' valleys at the corners of the Brillouin zone as shown in Figure 7a. These K and K' (or -K) valleys are separated by a big momentum space, offering low-energy carriers another degree of freedom. The occupation of the different valley (K or K') could be used as a representation of binary-value states. One may manipulate the valley degree of freedom for information operations in a similar way as in spintronics, which leads to the conceptual "valleytronics". Owing to the inversion symmetry breaking, there exist non-zero but contrasting orbital magnetic moments at K and K' valleys in monolayer TMDs.<sup>6,7</sup> These contrasting orbital magnetic moments at K and K' valleys provide a knob to manipulate the valley degree of freedom. This quantum manipulation could be realized either by electric means, for instance, via valley Hall effects<sup>6,24</sup> which is analogous to spin Hall effects, or by optical ways.<sup>7-9</sup> It was predicted that there are valley dependent interband optical selection rules at K/K' valleys due to the contrasting orbital magnetic moments and as well the requirement of conservation in angular momentum.<sup>6,7</sup> The optical transitions at K and K' valleys have the contrasting circular helicity, i.e., the right(left)-handed circularly polarized light corresponds to the optical transition at K(K') valley. The valley dependent optical selection rules provide a protocol to address the valley polarization in monolayer TMDs.

As a result of the spin-orbit coupling and time reversal symmetry, the Zeeman like spin splitting at valence band edges has the opposite sign between K and K' valleys at monolayer TMDs as illustrated in Figure 7b. The Kramer doublet, spin-up state at K valley  $|K \uparrow\rangle$  and spin-down state at K' valley  $|K' \downarrow\rangle$ , are separated from the other

doublet  $|K' \uparrow\rangle$  and  $|K \downarrow\rangle$  by the SOC energy which is around 0.16eV for molybdenum dichalcogenides and around 0.4eV for tungsten dichalcogenides. This strong SOC and explicit inversion symmetry breaking lock the spin and valley degrees of freedom in 2D TMDs and this interplay leads to sophisticated consequences. First, spin and valley relaxation are greatly suppressed at the valence band edges as an extra necessity of both spin flip and intervalley scattering has to be satisfied for holes' relaxation in monolayer TMDs. Second, the valley polarization often leads to spin polarization in monolayer TMDs and vice versa.

Valley polarization in monolayer TMDs can be easily achieved by controlling the polarization of the optical excitation, which has been demonstrated in polarization resolved photoluminescence measurements.<sup>7-9, 23</sup> The valley dependent optical selection rules suggest optical circular dichroism in the PL spectrum. In other words, if the monolayer TMD is excited with circularly polarized light sources the PL will carry the same circular polarization with that of the excitation. This circular dichroism of the PL has been reported in all monolayer TMDs (MoS<sub>2</sub>, WS<sub>2</sub>, WSe<sub>2</sub>, and MoSe<sub>2</sub>). The behavior is exhibited in an example of the polarization sensitive PL spectrum taken on monolayer WS<sub>2</sub> under near resonance conditions at low temperature, as shown in Figure 7c. The PL of monolayer WS<sub>2</sub> exactly follows the helicities of the exciting laser source. The universal definition for the degree of circular polarization  $P = \frac{I(\sigma+) - I(\sigma-)}{I(\sigma+) + I(\sigma-)}$ , where  $I(\sigma+)/I(\sigma-)$  is the intensity of the right/left handed circular component of the PL, could be used to quantitatively evaluate the valley polarization. The degree of circular polarization of the PL on

monolayer TMDs is roughly constant around the peak position in the PL spectrum, independent of inhomogeneous broadening. At early stage of the study on valley polarization in monolayer MoS<sub>2</sub>, the circular polarization P was found to be with relatively low values,<sup>7, 8</sup> which were in contrast to the theoretical prediction for the validity of fully valley polarization. The deviation might result from the poor sample quality and the effect of substrates,<sup>3</sup> which act as atomic scattering centers. The atomic scattering centers waive the requirement of crystal momentum conservation and dramatically increase the intervalley scattering which is the channel for depolarization. This leads to the significant valley depolarization in monolayer TMDs. Experimental findings show that atomically flat boron nitride (BN) substrate or the improved quality of the crystals could lead to near unity valley polarization in monolayer TMD.<sup>3, 49</sup> In addition, the valley polarization measured by the steady-state PL gives an estimate on the valley lifetime as the circular polarization P is determined by the relation of the excited state lifetime and the valley relaxation time. If a circularly polarized light pumps K valley only, the dynamics of the exciton density ( $N_K$  and  $N_{-K}$  on K and -K valleys) can be described by the following equations

$$\frac{dN_K}{dt} = -\frac{N_K}{\tau} - \left(\frac{N_K}{\tau_K} - \frac{N_{-K}}{\tau_K}\right) + C = 0 \quad \text{and} \quad \frac{dN_{-K}}{dt} = -\frac{N_{-K}}{\tau} + \left(\frac{N_K}{\tau_K} - \frac{N_{-K}}{\tau_K}\right) = 0,$$

where  $\tau$  is the exciton life time at both K and -K valleys,  $\tau_K^{-1}$  is the  $K \leftrightarrow -K$  intervalley scattering rate and C is the exciton generation rate. At steady-state,  $\frac{dN_K}{dt} = \frac{dN_{-K}}{dt} = 0$ .

The dependence of the degree of PL circular polarization P on the steady-state density of excitons ( $N_K$  and  $N_{-K}$ ) can be thus described as  $P = \frac{N_K - N_{-K}}{N_K + N_{-K}} = \frac{P_0}{1 + 2\tau/\tau_K}$ . Valley life

time  $\tau_K$  could be then inferred from the measured PL circular polarization. The

observed values for valley polarization in monolayer MoS<sub>2</sub> by different groups,<sup>7-9, 49</sup> ranging from 30% to near unity, indicate that valley can have a longer life time than that of photo-excited carriers, which is one of the prerequisites for practical device applications.

The validity of the valley degree of freedom in monolayer TMDs can be checked by the well-known Hanle effect.<sup>8, 50</sup> The need of the verification for valley dependent optical selection rules lies in that in many group III-V semiconductors there exist spin dependent optical selection rules, which enable the spin polarization and result in the circular polarization of PL under circularly polarized excitations. It is therefore necessary to clarify that the observed circularly polarized PL in monolayer TMDs originates from valley-dependent other than spin-dependent optical selection rules. This could be done by applying a transverse magnetic field and monitoring the change of the PL helicity. The rotation symmetry protects the spin pointing along the c axis (out-of-plane) direction. An in-plane magnetic field will cause the spin to precess around the applied field, leading to significant decrease of the spin component projected in the direction of c axis. In contrast, the valley index is immune to such a transverse magnetic field as there is no direct coupling between the two. Consequently, the measured PL circular polarization in a transverse magnetic field would be greatly suppressed if it is from spin-dependent instead of valley-dependent selection rules, which can be foreseen in standard Hanle experiments. However, the circular polarization of the PL in monolayer MoS<sub>2</sub> was found to be strongly robust against the transverse magnetic field.<sup>8, 50</sup> The constant PL polarization could persist in magnetic

fields up to 9T as demonstrated in Figure 8. The robustness of the PL polarization confirms that the valley polarization is the origin of the circularly polarized PL in monolayer TMDs and it manifests the existence of the valley degree of freedom.

Further proof for valley degree of freedom in TMD monolayers is demonstrated by the electrical tuning of the inversion symmetry in bilayer MoS<sub>2</sub>. The valley dependent optical selection rules arise from the inversion symmetry breaking in monolayers.<sup>6</sup> Nevertheless, in bilayer MoS<sub>2</sub>, the 2H stacking order restore the inversion symmetry, leading to the invalidation of valley selective optical selection rules. As a result, the PL from the direct interband optical transitions at K/K' valleys in bilayers should be unpolarized, which has been observed in pristine bilayer MoS<sub>2</sub>.<sup>8</sup> However, the crystal inversion symmetry can be broken by an out-of-plane electrical field which could come from either external electric gating or interface charging. The interactions with the substrates including charge transfers or photo-doping often break the inversion symmetry to some extent and induce a finite circular dichroism in bilayer MoS<sub>2</sub>. The electric gating provides a route to break the inversion symmetry in a control way and induce valley contrasting magnetic moments and optical selection rules in bilayers. The first demonstration of electrical control on inversion symmetry has been done by Wu et al<sup>26</sup> through studying the gate voltage dependence of the PL polarization from bilayer MoS<sub>2</sub> in a field-effect-transistor like device. Very recently the in-plane electric field induced circularly polarized band-edge electroluminescence has been reported in monolayer and multilayer WSe<sub>2</sub>.<sup>27</sup> It demonstrates a pure electric way to manipulate the valley degree of freedom.

Another intriguing feature in monolayer TMDs is the possibility of coherently manipulating light-matter interaction via valley coherence. In monolayer TMDs, the state  $|K \uparrow\rangle$  at K valley and  $|K' \downarrow\rangle$  at K' valley are time-reversal images to each other. The quantum trajectories of hot carrier relaxation via intravalley scatterings are the same for both channels at K and K' valleys.<sup>23</sup> This is experimentally demonstrated in monolayer WSe<sub>2</sub> by the linearly polarized PL experiments.<sup>23</sup> The linearly polarized light could be treated as a coherent superposition of right- and left-handed circularly polarized lights. Hot carriers generated by linearly polarized excitation at K and K' valleys relax to the band-edge via intravalley scatterings of phonons and Coulomb interactions, which share the same quantum trajectories and keep the same phase difference. So the polarization of the band-edge excitons exactly follows that of excitation source. The ability of addressing valley coherence raises the possibility of coherent manipulation of quantum states via light-matter interactions in 2D TMDs.

### ***3.2 Optical signature of spin-valley coupling in multilayer TMDs***

In bilayer TMDs, the inversion symmetry is explicitly restored as the consequence of Bernal stacking sequence. It is demonstrated by the negligible SHG in bilayer TMDs. However, if the spin-orbit coupling is taken into account, the valley physics can survive even in inversion-symmetric even-layer TMDs. In the  $2H$  packing order, each layer is a  $\pi$  rotation of each other and it switches K and K' valleys but leaves the spin unchanged, which results in a sign change for the spin-valley coupling from layer to layer as illustrated in Figure 9. The spin in the same valley of adjacent layers points to opposite orientation. In MoS<sub>2</sub> the SOC is found to be around 0.16eV, close to the

interlayer hopping energy of around 0.1eV. And the SOC is not strong enough to suppress the interlayer coupling at K/K' valleys. This is the reason that the circular dichroism disappears in pristine bilayer MoS<sub>2</sub>. One could also tune the inversion symmetry breaking in bilayer MoS<sub>2</sub> with an external out-of-planer electric field.<sup>26</sup> In contrast, the SOC in tungsten dichalcogenides is around 0.4eV, much larger than the interlayer hopping energy. Consequently, the interlayer coupling at K valley is fully suppressed by the SOC in tungsten dichalcogenides. So the valley dependent optical selection rules demonstrated in monolayers extend to bilayer/multilayer tungsten dichalcogenides, though only valid for optical transitions at K/K' valley. As spin-valley coupling has the opposite sign between each layer, the circular dichroism corresponds to the real spin polarization in bilayer. Namely the left(right)-handed circular polarization is associated with optical transitions with  $|K \uparrow_u\rangle$  and  $|K' \uparrow_l\rangle$  ( $|K \downarrow_u\rangle$  and  $|K' \downarrow_l\rangle$ ) as sketched in Figure 9c, where *u* and *l* denotes the upper and lower layers respectively, indicating the extra layer degree of freedom in bilayers. The interplay of valley, spin and layer degrees of freedom stimulates proposals of quantum manipulation via electric and magnetic means.<sup>25</sup> As the spin-valley coupling is particularly pronounced in atomically thin tungsten dichalcogenides, optical study on bilayer WS<sub>2</sub> and WSe<sub>2</sub> is more appealing for valley and spin related physics.

Initial experimental hint on the suppression of interlayer hopping for carriers in K/K' valleys by spin-valley coupling in multilayer WX<sub>2</sub> come from the observation of constant A-B splitting pattern in the PL spectra.<sup>15, 31</sup> The A and B excitons originate from the Zeeman-like spin splitting in the valence band and the energy difference

between A and B excitons reflects the SOC strength. The energy difference of the A and B excitonic transitions in multilayer tungsten dichalcogenides is same as that in monolayer with an almost constant value of 0.4eV (Figure 10a and 10b: example of multilayer WS<sub>2</sub>). The observed constant A-B splitting pattern is an evidence of the suppression of interlayer coupling around K/K' valleys, as the interlayer coupling if any inevitably modify the splitting pattern and splitting strength.<sup>15</sup> The spin and valley indices of carriers in K/K' valleys in multilayer WX<sub>2</sub> are locked to specific layers, which can be seen from the density distribution of the wavefunction for states at K or K' valley (Figure 10c). The direct evidence of the coupling of valley, spin, and layer degrees of freedom in 2D TMDs lies in the robust circular dichroism observed in bilayer WS<sub>2</sub>, as sampled in Figure 11, where the degree of circular polarization of the PL from bilayer WS<sub>2</sub> is significantly higher than that of monolayers.<sup>28</sup> The robust circular dichroism is the consequence of interplays among spin, valley, and layer degrees of freedoms, though the detailed mechanism is not clear yet. Besides, the bilayer WS<sub>2</sub> demonstrated robust valley coherence even at room temperature.<sup>28</sup>

#### ***4. Summary and Outlook***

Atomically thin TMD crystals feature a family of intrinsic 2D semiconductors well recognized as promising candidates for ultimate electronics and optoelectronics. Vast research efforts have revealed strong Coulomb interactions, valley related physics, giant spin-orbit coupling, spin-valley coupling, etc. in the 2D TMDs. These unique properties make 2D TMDs an unprecedented platform for the practice of quantum manipulations, valleytronics and spintronics. Besides, the interplay of light-matter

interactions, spin, valley, and layer degrees of freedoms in 2D TMDs particularly in 2D tungsten dichalcogenides, raises numerous inspirations of novel quantum manipulations, charge/magnetism sensing beyond physics.

One of the annoying bottlenecks for aspects in fundamental researches and the preliminary study on quantum manipulations lies in the imperfect sample quality. One of the subsequent phenomena is the broad linewidth of the photoluminescence spectra among which the best value, around 5meV at temperature of 15K, comes from exfoliated monolayer MoSe<sub>2</sub>, in contrast with the narrow linewidth of a fraction of 1meV in GaAs quantum wells. The broad linewidth reflects a strong inhomogeneous broadening due to tremendous defect/imperfection scatterings. The defects and imperfections blur the intrinsic information and modify the properties usually in a negative way. This is likely to be solved with the progress by chemists and material scientists. Another potentially attracting research direction in 2D TMDs is the material engineering on their crystal structure. At current stage, most research efforts are devoted to TMDs with *2H* stacking order. For layered material, it is also possible to have other crystallographic phases, for instance, *1T* or *3R*. The change of the packing order in 2D multilayer TMDs will bring extraordinary optical and electrical properties, i.e. the *3R* stacking order will keep the inversion asymmetry in multilayer and bulk TMDs which means the valley and spin physics can be developed to even bulk samples. This will provide rich research opportunities in various fields.

**Acknowledgement.** H Zeng would like to thank the support from the Direct Grant

for research 2014/2015 in the Chinese University of Hong Kong. X Cui acknowledges the support from Area of Excellency (AoE/P-04/08), Strategic Research Theme on New Materials, and HKU9/CRF/13G of Hong Kong Research Grant Council.

## Reference

1. K. S. Novoselov, A. K. Geim, S. V. Morozov, D. Jiang, Y. Zhang, S. V. Dubonos, I. V. Grigorieva and A. A. Firsov, *Science*, 2004, **306**, 666-669.
2. Y. Zhang, Y.-W. Tan, H. L. Stormer and P. Kim, *Nature*, 2005, **438**, 201-204.
3. K. F. Mak, C. Lee, J. Hone, J. Shan and T. F. Heinz, *Physical Review Letters*, 2010, **105**, 136805.
4. A. Splendiani, L. Sun, Y. Zhang, T. Li, J. Kim, C.-Y. Chim, G. Galli and F. Wang, *Nano Letters*, 2010, **10**, 1271-1275.
5. RadisavljevicB, RadenovicA, BrivioJ, GiacomettiV and KisA, *Nat Nano*, 2011, **6**, 147-150.
6. D. Xiao, G.-B. Liu, W. Feng, X. Xu and W. Yao, *Physical Review Letters*, 2012, **108**, 196802.
7. T. Cao, G. Wang, W. Han, H. Ye, C. Zhu, J. Shi, Q. Niu, P. Tan, E. Wang, B. Liu and J. Feng, *Nat Commun*, 2012, **3**, 887.
8. H. Zeng, J. Dai, W. Yao, D. Xiao and X. Cui, *Nat Nano*, 2012, **7**, 490-493.
9. K. F. Mak, K. He, J. Shan and T. F. Heinz, *Nat Nano*, 2012, **7**, 494-498.
10. M. Chhowalla, H. S. Shin, G. Eda, L.-J. Li, K. P. Loh and H. Zhang, *Nat Chem*, 2013, **5**, 263-275.
11. K. S. Novoselov, D. Jiang, F. Schedin, T. J. Booth, V. V. Khotkevich, S. V. Morozov and A. K. Geim, *Proceedings of the National Academy of Sciences of the United States of America*, 2005, **102**, 10451-10453.
12. K.-K. Liu, W. Zhang, Y.-H. Lee, Y.-C. Lin, M.-T. Chang, C.-Y. Su, C.-S. Chang, H. Li, Y. Shi, H. Zhang, C.-S. Lai and L.-J. Li, *Nano Letters*, 2012, **12**, 1538-1544.
13. J. N. Coleman, M. Lotya, A. O'Neill, S. D. Bergin, P. J. King, U. Khan, K. Young, A. Gaucher, S. De, R. J. Smith, I. V. Shvets, S. K. Arora, G. Stanton, H.-Y. Kim, K. Lee, G. T. Kim, G. S. Duesberg, T. Hallam, J. J. Boland, J. J. Wang, J. F. Donegan, J. C. Grunlan, G. Moriarty, A. Shmeliov, R. J. Nicholls, J. M. Perkins, E. M. Grieverson, K. Theuwissen, D. W. McComb, P. D. Nellist and V. Nicolosi, *Science*, 2011, **331**, 568-571.
14. C. Lee, H. Yan, L. E. Brus, T. F. Heinz, J. Hone and S. Ryu, *ACS Nano*, 2010, **4**, 2695-2700.
15. H. Zeng, G.-B. Liu, J. Dai, Y. Yan, B. Zhu, R. He, L. Xie, S. Xu, X. Chen, W. Yao and X. Cui, *Sci. Rep.*, 2013, **3**, 1608.

16. H. Zeng, B. Zhu, K. Liu, J. Fan, X. Cui and Q. M. Zhang, *Physical Review B*, 2012, **86**, 241301.
17. G. Plechinger, S. Heydrich, J. Eroms, D. Weiss, C. Schüller and T. Korn, *Applied Physics Letters*, 2012, **101**, 101906.
18. X. Zhang, W. P. Han, J. B. Wu, S. Milana, Y. Lu, Q. Q. Li, A. C. Ferrari and P. H. Tan, *Physical Review B*, 2013, **87**, 115413.
19. Y. Zhao, X. Luo, H. Li, J. Zhang, P. T. Araujo, C. K. Gan, J. Wu, H. Zhang, S. Y. Quek, M. S. Dresselhaus and Q. Xiong, *Nano Letters*, 2013, **13**, 1007-1015.
20. N. Kumar, S. Najmaei, Q. Cui, F. Ceballos, P. M. Ajayan, J. Lou and H. Zhao, *Physical Review B*, 2013, **87**, 161403.
21. Y. Li, Y. Rao, K. F. Mak, Y. You, S. Wang, C. R. Dean and T. F. Heinz, *Nano Letters*, 2013, **13**, 3329-3333.
22. X. Yin, Z. Ye, D. A. Chenet, Y. Ye, K. O'Brien, J. C. Hone and X. Zhang, *Science*, 2014, **344**, 488-490.
23. A. M. Jones, H. Yu, N. J. Ghimire, S. Wu, G. Aivazian, J. S. Ross, B. Zhao, J. Yan, D. G. Mandrus, D. Xiao, W. Yao and X. Xu, *Nat Nano*, 2013, **8**, 634-638.
24. K. F. Mak, K. L. McGill, J. Park and P. L. McEuen, *Science*, 2014, **344**, 1489-1492.
25. Z. Gong, G.-B. Liu, H. Yu, D. Xiao, X. Cui, X. Xu and W. Yao, *Nat Commun* 2013, **4**, 2053.
26. S. Wu, J. S. Ross, G.-B. Liu, G. Aivazian, A. Jones, Z. Fei, W. Zhu, D. Xiao, W. Yao, D. Cobden and X. Xu, *Nat Phys*, 2013, **9**, 149-153.
27. Y. J. Zhang, T. Oka, R. Suzuki, J. T. Ye and Y. Iwasa, *Science*, 2014, **344**, 725-728.
28. B. Zhu, H. Zeng, J. Dai, Z. Gong and X. Cui, *Proceedings of the National Academy of Sciences*, 2014.
29. G. Eda, H. Yamaguchi, D. Voiry, T. Fujita, M. Chen and M. Chhowalla, *Nano Letters*, 2011, **11**, 5111-5116.
30. T. Li and G. Galli, *The Journal of Physical Chemistry C*, 2007, **111**, 16192-16196.
31. W. Zhao, Z. Ghorannevis, L. Chu, M. Toh, C. Kloc, P.-H. Tan and G. Eda, *ACS Nano*, 2012, **7**, 791-797.
32. A. Kuc, N. Zibouche and T. Heine, *Physical Review B*, 2011, **83**, 245213.
33. D. Voiry, A. Goswami, R. Kappera, e. SilvaCecilia de Carvalho Castro, D. Kaplan, T. Fujita, M. Chen, T. Asefa and M. Chhowalla, *Nat Chem*, 2015, **7**, 45-49.
34. F. K. Perkins, A. L. Friedman, E. Cobas, P. M. Campbell, G. G. Jernigan and B. T. Jonker, *Nano Letters*, 2013, **13**, 668-673.
35. Z. Y. Zhu, Y. C. Cheng and U. Schwingenschlögl, *Physical Review B*, 2011, **84**, 153402.
36. J. S. Ross, S. Wu, H. Yu, N. J. Ghimire, A. M. Jones, G. Aivazian, J. Yan, D. G. Mandrus, D. Xiao, W. Yao and X. Xu, *Nat Commun*, 2013, **4**, 1474.
37. J. A. Schuller, S. Karaveli, T. Schiros, K. He, S. Yang, I. Kymissis, J. Shan and R. Zia, *Nat Nano*, 2013, **8**, 271-276.
38. K. F. Mak, K. He, C. Lee, G. H. Lee, J. Hone, T. F. Heinz and J. Shan, *Nat Mater*, 2013, **12**, 207-211.
39. A. Chernikov, T. C. Berkelbach, H. M. Hill, A. Rigosi, Y. Li, O. B. Aslan, D. R. Reichman, M. S. Hybertsen and T. F. Heinz, *Physical Review Letters*, 2014, **113**, 076802.
40. A. Shimizu, T. Ogawa and H. Sakaki, *Physical Review B*, 1992, **45**, 11338-11341.
41. K. He, N. Kumar, L. Zhao, Z. Wang, K. F. Mak, H. Zhao and J. Shan, *Physical Review Letters*,

- 2014, **113**, 026803.
42. M. M. Ugeda, A. J. Bradley, S.-F. Shi, F. H. da Jornada, Y. Zhang, D. Y. Qiu, W. Ruan, S.-K. Mo, Z. Hussain, Z.-X. Shen, F. Wang, S. G. Louie and M. F. Crommie, *Nat Mater*, 2014, **13**, 1091-1095.
  43. Z. Ye, T. Cao, K. O'Brien, H. Zhu, X. Yin, Y. Wang, S. G. Louie and X. Zhang, *Nature*, 2014, **513**, 214-218.
  44. B. Zhu, X. Chen and X. Cui, *Sci Rep.*, 2015, 5, 9218.
  45. H.-P. Komsa and A. V. Krasheninnikov, *Physical Review B*, 2012, **86**, 241201.
  46. A. Ramasubramaniam, *Physical Review B*, 2012, **86**, 115409.
  47. A. R. Klots, A. K. M. Newaz, B. Wang, D. Prasai, H. Krzyzanowska, J. Lin, D. Caudel, N. J. Ghimire, J. Yan, B. L. Ivanov, K. A. Velizhanin, A. Burger, D. G. Mandrus, N. H. Tolk, S. T. Pantelides and K. I. Bolotin, *Sci. Rep.*, 2014, **4**.
  48. G. Wang, X. Marie, I. Gerber, T. Amand, D. Lagarde, L. Bouet, M. Vidal, A. Balocchi and B. Urbaszek, *Physical Review Letters*, 2015, **114**, 097403.
  49. S. Wu, C. Huang, G. Aivazian, J. S. Ross, D. H. Cobden and X. Xu, *ACS Nano*, 2013, **7**, 2768-2772.
  50. G. Sallen, L. Bouet, X. Marie, G. Wang, C. R. Zhu, W. P. Han, Y. Lu, P. H. Tan, T. Amand, B. L. Liu and B. Urbaszek, *Physical Review B*, 2012, **86**, 081301.

## Figures

Figure 1. Schematic of the lattice structure of bulk and monolayer TMDs.

(a). Top view of monolayer TMD crystal (left) and the unit cell (right), which clearly shows the spatial inversion symmetry breaking in monolayers; (b). Schematic of bulk and even-layer  $\text{MX}_2$  structure (left) and the unit cell (right), which has the inversion center located at the middle plane.

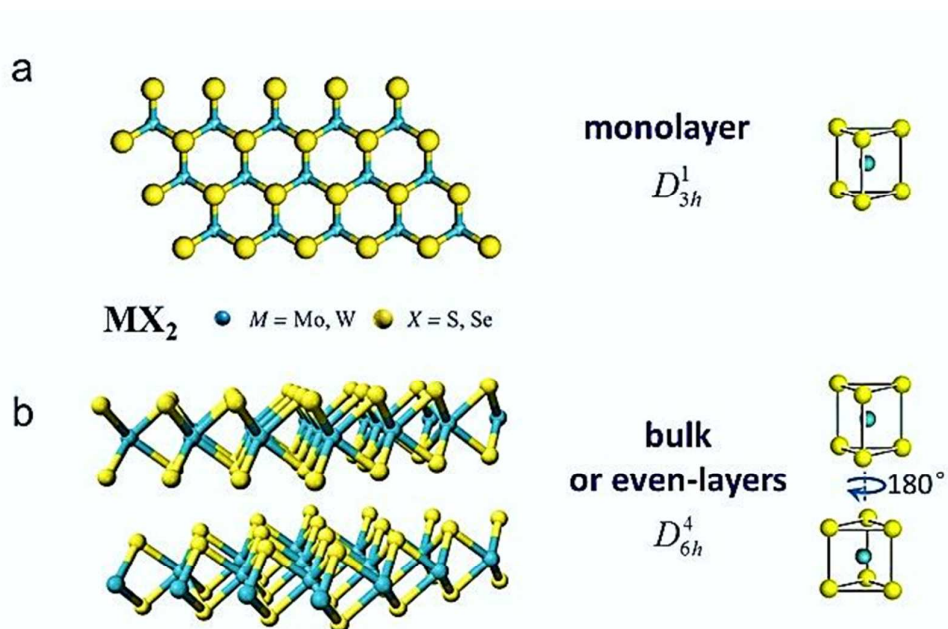


Figure 2. Electronic properties of atomically thin TMD layers.

(a). Calculated band structures of bulk, bilayer, and monolayer MoS<sub>2</sub>. The Fermi level is indicated by dashed red lines. The arrows indicate the fundamental band-gap (direct or indirect) for a given system. (Courtesy of Ref. 32); (b). Photoluminescence spectra of monolayer and bilayer MoS<sub>2</sub> in the visible range. Inset: the PL quantum yield dependence on the sample thickness (number of unit layers). (Courtesy of Ref. 3); (c). Evolution of the band-gap energy of thin layers of MoS<sub>2</sub>. The dashed line represents the (indirect) band-gap energy of bulk sample. (Courtesy of Ref. 3); (d). Calculated band structures of bulk, bilayer, and monolayer WS<sub>2</sub>. (Courtesy of Ref. 32) The Fermi level is indicated by dashed red lines. The arrows indicate the fundamental band-gap (direct or indirect) for a given system; (e). PL spectra of monolayer and bilayer WS<sub>2</sub>. Inset: relative PL intensity of multilayer WS<sub>2</sub> as a function of film thickness under the same conditions (normalized by the PL intensity of monolayer at 1). (Courtesy of Ref. 15); (f). The band-gap as a function of the film thickness in WS<sub>2</sub>. (Courtesy of Ref. 15)

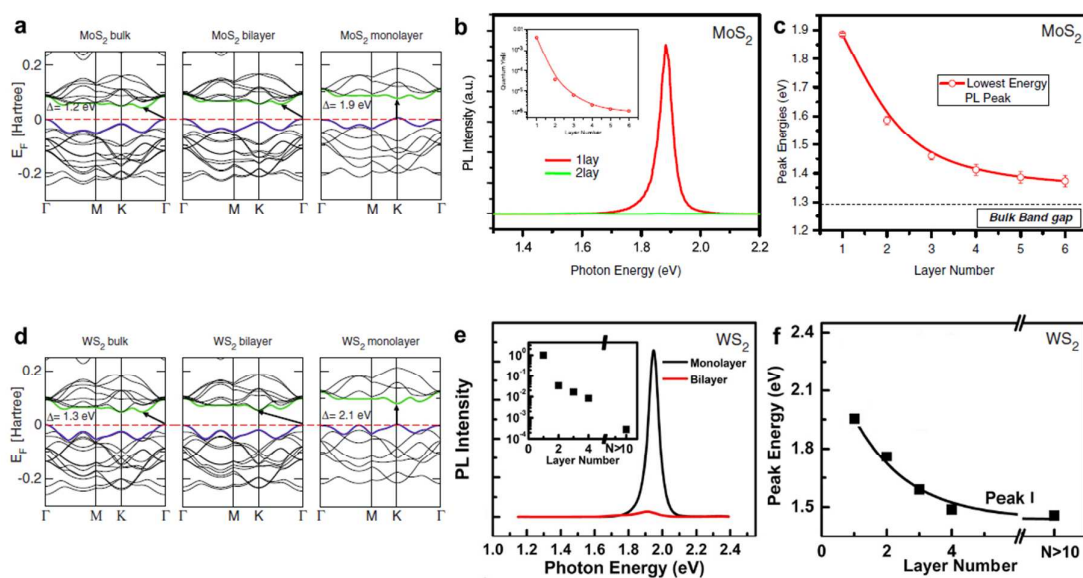


Figure 3. Optical signatures of spin-orbit coupling in monolayer TMDs. (Courtesy of Ref. 36)

(a). Band structure of monolayer  $\text{MoSe}_2$  calculated by DFT with the correction of SOC. The arrows in red and blue indicate the A and B direct-band-gap excitonic transitions respectively. The valence band at K point shows a splitting of 180 meV; (b). Low temperature (20K) differential reflectance spectrum. The sharp peaks labelled as A and B correspond to the band-edge excitons originating from spin-split valence bands at K point.

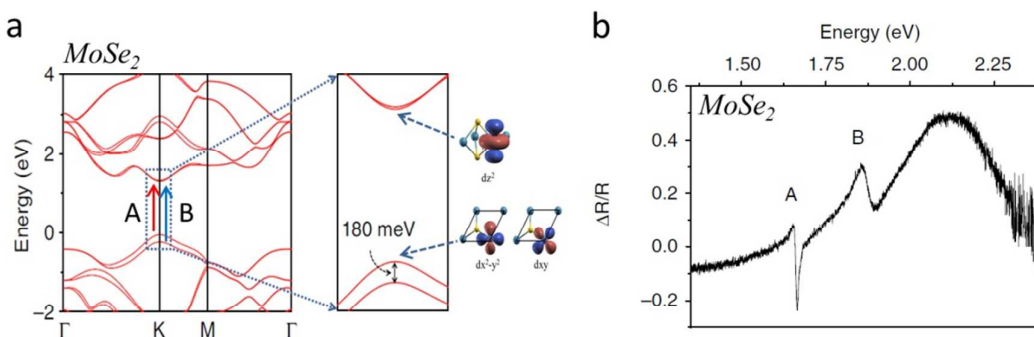


Figure 4. Raman scattering spectroscopy on TMDs.

(a). Schematic of four Raman-active modes in 2D TMDs; (b). Raman spectra of thin (few-layer) and bulk MoS<sub>2</sub> films. (Courtesy of Ref. 14); (c). Frequencies of  $A_{1g}$  and  $E_{2g}^1$  Raman modes (left vertical axis) and their difference (right vertical axis) as a function of layer thickness. (Courtesy of Ref. 14); (d). Raman spectra of few-layer MoS<sub>2</sub> in low-frequency range. (Courtesy of Ref. 16); (e). Thickness dependence of the  $E_{2g}^2$  shear mode (upper panel) and the  $B_{2g}^2$  LBM or compression mode (lower panel) for few-layer MoS<sub>2</sub>. The blue curve is the fitting with the linear chain model. The red and green curves are produced with least-squares fitting. (Courtesy of Ref. 16)

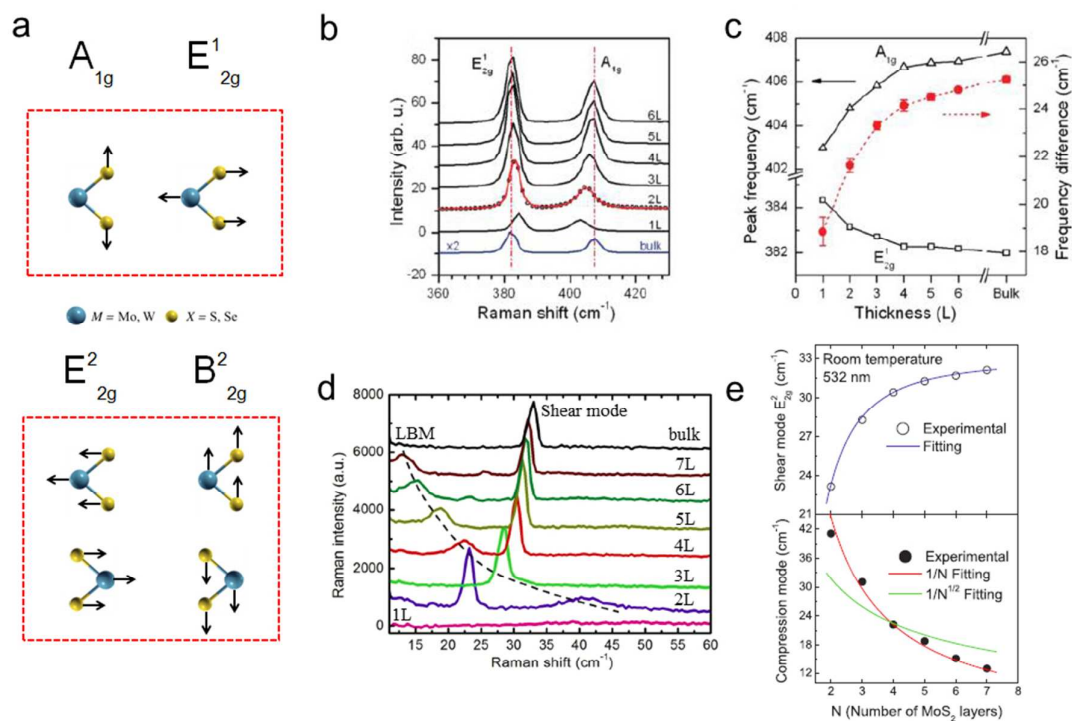


Figure 5. SHG in monolayer and multilayer TMDs. (a)-(d): Courtesy of Ref 15; and (e)-(h): Courtesy of Ref 22.

(a). Optical image of mechanically exfoliated monolayer and multilayer  $WS_2$  on Si/SiO<sub>2</sub> substrate; (b). Photoluminescence-mapping image at the direct-gap transition. Only monolayers are visible at the present contrast due to much higher PL yield; (c). The corresponding SHG on the same sample. The highest intensity labelled in red arises from monolayers; (d) Relative SHG intensity as a function of the film thickness in  $WS_2$ . The SHG intensity shows an even-odd oscillation dependence on the film thickness; (e). Optical image of a large area of CVD-grown monolayer  $MoS_2$ ; (f). SHG image of a polycrystalline monolayer  $MoS_2$  of the same area. The grains and grain boundaries are clearly revealed by the reduced SHG intensity; (g). The direct crystal orientation image shows the crystal orientations of the irregular-shaped polycrystalline aggregates; (h). Schematics show the flakes I and II are two crystals with opposite orientations, as they have the same contrast in crystal orientation maps but a strongly destructive interference boundary. Crystals II and III show an orientation mismatch of  $\sim 12^\circ$ . The crystal groups a and b show two cyclic twin boundaries with  $60^\circ$  and  $30^\circ$ , respectively.

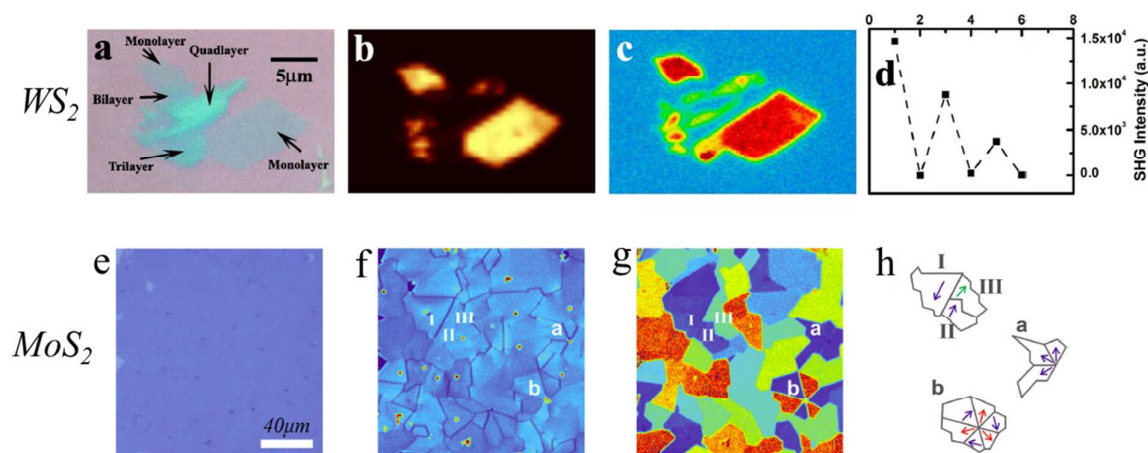


Figure 6. Electrostatic control of exciton and trion states in 2D TMDs.

(a),(b). Absorption and photoluminescence spectra of monolayer MoS<sub>2</sub> at different back-gate voltages. Both the neutral exciton (A) and trion (A<sup>-</sup>) features (with the corresponding resonance energies indicated by the dashed lines) can be identified. (Courtesy of Ref. 38); (c). Color contour plot of normalized PL spectra in monolayer MoSe<sub>2</sub> under various back-gate bias. Free excitons, electron-bound excitons (negatively charged trions) and hole-bound excitons (positively charged trions) are labeled with X<sup>0</sup>, X<sup>-</sup>, and X<sup>+</sup>, respectively. (Courtesy of Ref. 36); (d). Illustration of the gate-dependent trion and exciton quasi-particles and transitions. (Courtesy of Ref. 36)

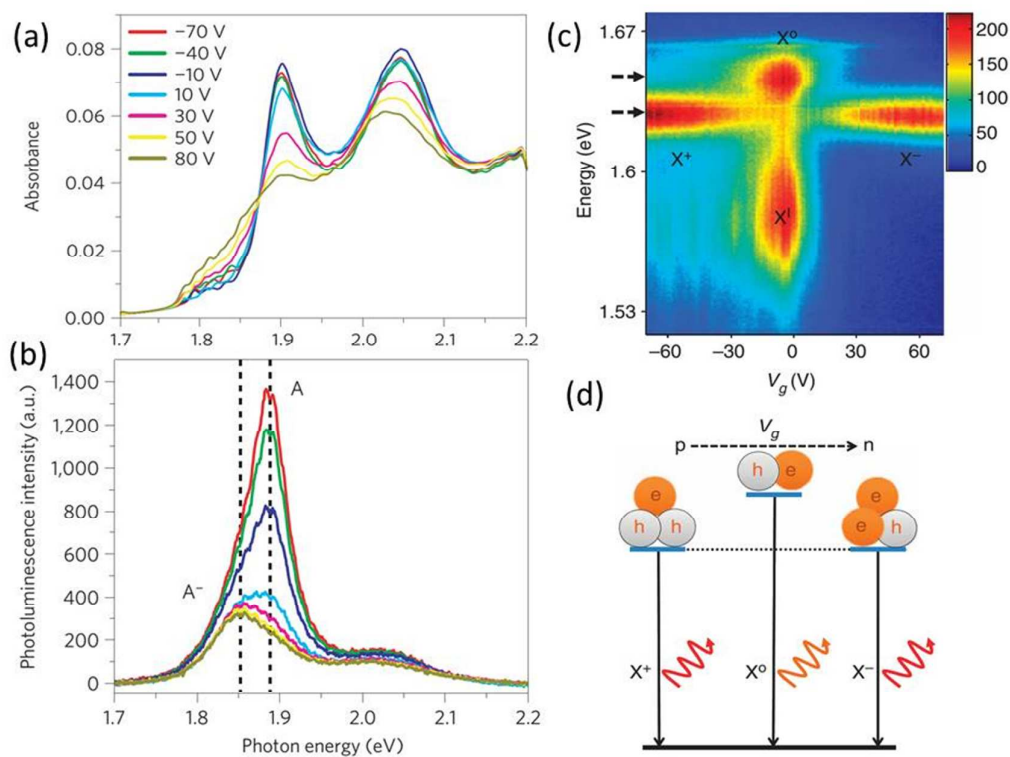


Figure 7. Valley-dependent optical transitions in monolayer TMDs.

(a). Schematic drawing of the band structure of monolayer TMDs at the band edges located at the K points. (Courtesy of Ref. 6); (b). Schematic of valley-dependent optical selection rules and the Zeeman-like spin splitting in the valence bands of monolayer TMDs. (Courtesy of Ref. 28); (c). Polarization resolved luminescence spectra of monolayer  $\text{WS}_2$  with  $\sigma_+$  detection (red) and  $\sigma_-$  detection (black) under near-resonant  $\sigma_+$  excitation (2.088 eV) at 10 K. Peak A is the excitonic transition at band edges of K (K') valleys. Inset presents the degree of the circular polarization at the prominent PL peak. (Courtesy of Ref. 28); (d). The degree of the circular polarization as a function of temperature. The curve (red) is a fit following a Boltzmann distribution where the intervalley scattering by phonons is assumed. (Courtesy of Ref. 28)

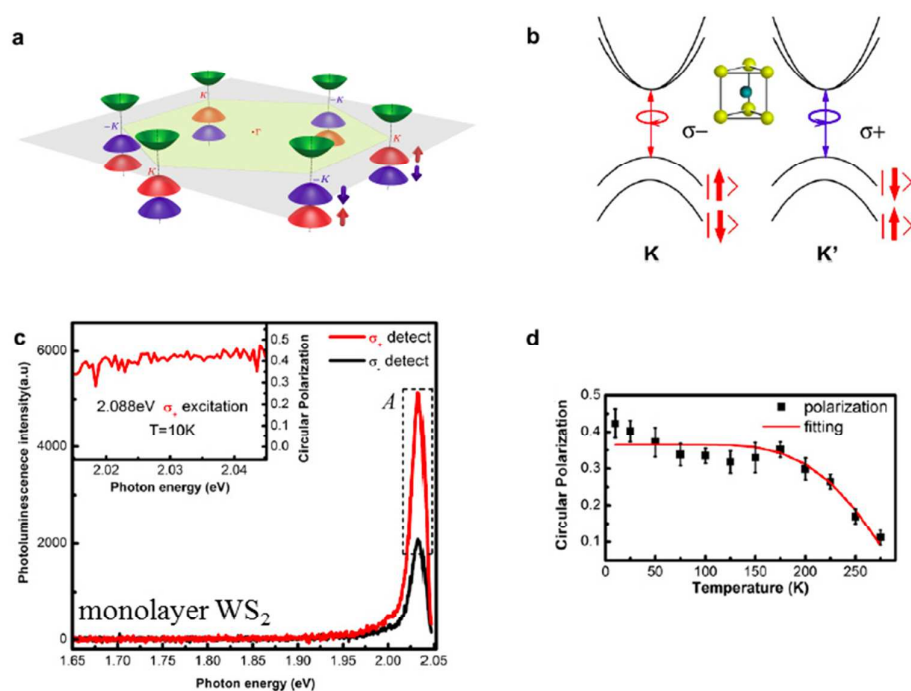


Figure 8. Hanle experiment on monolayer TMDs. (Courtesy of Ref. 50)

(a). Comparison of PL spectra of monolayer MoS<sub>2</sub> recorded for a transverse magnetic field  $B_T = 0, 4.5,$  and  $8.5\text{T}$  under otherwise identical experimental conditions using HeNe laser at  $1.96\text{eV}$ . Inset: Experimental geometry; (b). Measured PL circular polarization degree of the A exciton as a function of the applied transverse magnetic field  $B_T$  at  $T = 4\text{K}$  (squares) and at  $T = 100\text{K}$  (circles).

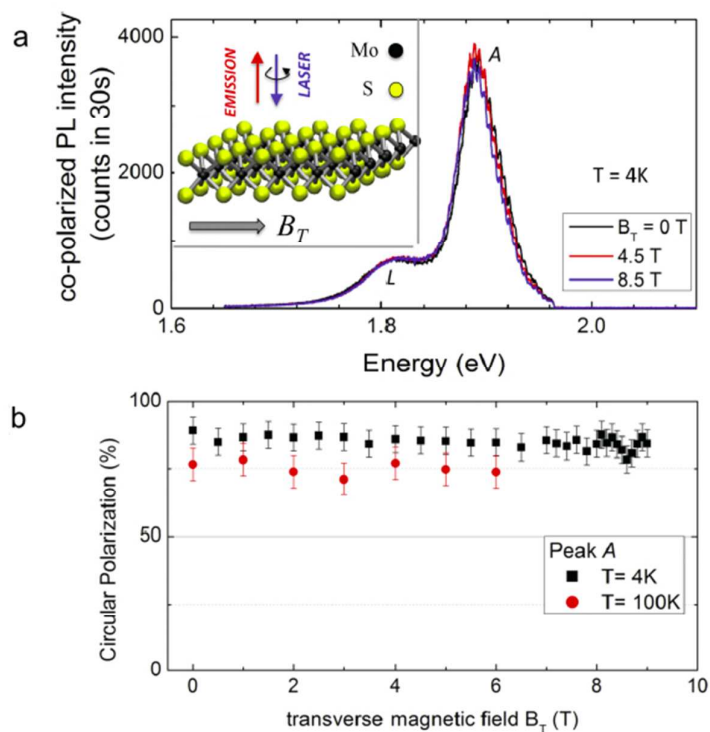


Figure 9. Structure and optical selection rules in Group-VI bilayer TMDs. (Courtesy of Ref. 25)

(a). Coordination structure of bilayer TMDs in Bernal stacking order; (b). Optical selection rules in decoupled monolayers with AB-stacking order. Dashed arrows indicate interlayer hopping; (c). Optical transition selection rules in the K and  $-K$  valleys of bilayers with interlayer hopping. The transitions denoted by the thick (thin) arrows have strength proportional to  $\cos 2\alpha$  ( $\sin 2\alpha$ ). The layer polarization of the Bloch states is schematically illustrated with the rectangular blocks where darker color denotes more occupation.

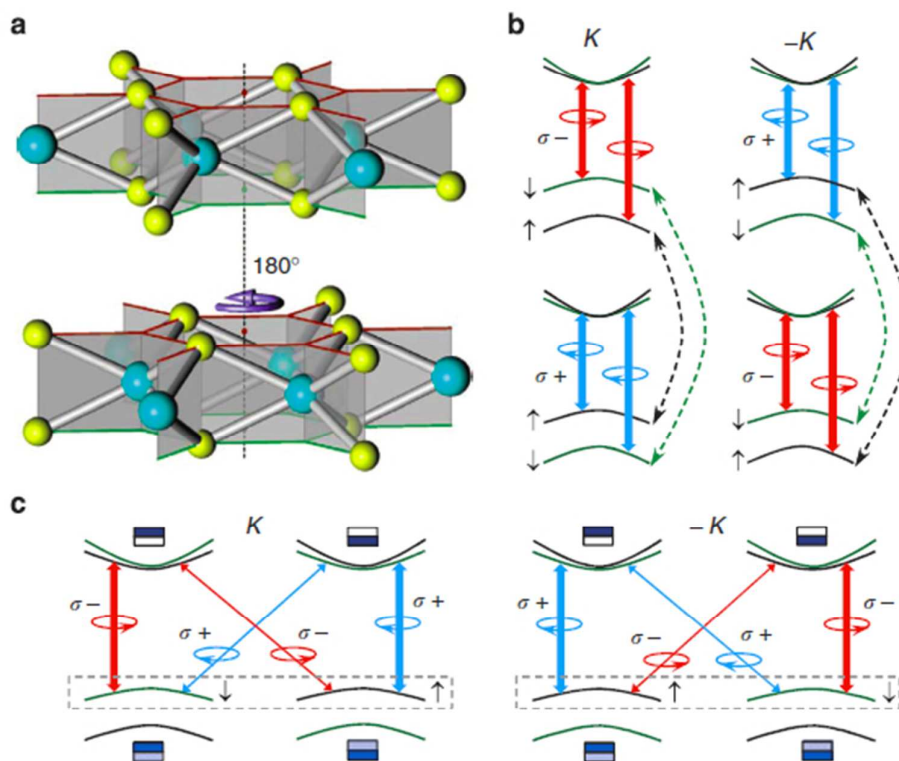


Figure 10. Optical signature of spin-valley coupling in multilayer TMDs. (Courtesy of Ref. 15)

(a). The normalized PL spectra (with respect to the peak A) of  $\text{WS}_2$  ultrathin films. I labels the luminescence from indirect gap interband transition, A and B label the direct-gap transitions from the split valence band edge to the conduction band edge at K points. Spectra (dash line) in the zoom windows have been multiplied by a factor as indicated for clarity; (b). The peak positions of I, A and B transitions as a function of the film thickness in  $\text{WS}_2$ . It shows an early constant energy difference of 0.4 eV which corresponds to the splitting of the valence band edge. The universal A-B splitting implies a suppression of interlayer hopping in tungsten dichalcogenides ultra-thin films; (c). Left: Diagram of spin-layer-valley coupling in  $2H$  stacked bilayer  $\text{WS}_2$ . Interlayer hopping is suppressed in bilayer  $\text{WS}_2$  owing to the coupling of spin, valley, and layer degrees of freedom. Right: Calculations show that in a given  $K'$  valley the wavefunction is fully spin polarized in the down state and almost fully localized in the bottom layer. The other degenerate state at the same  $K'$  point can be obtained by a spatial inversion plus a time reversal operation.

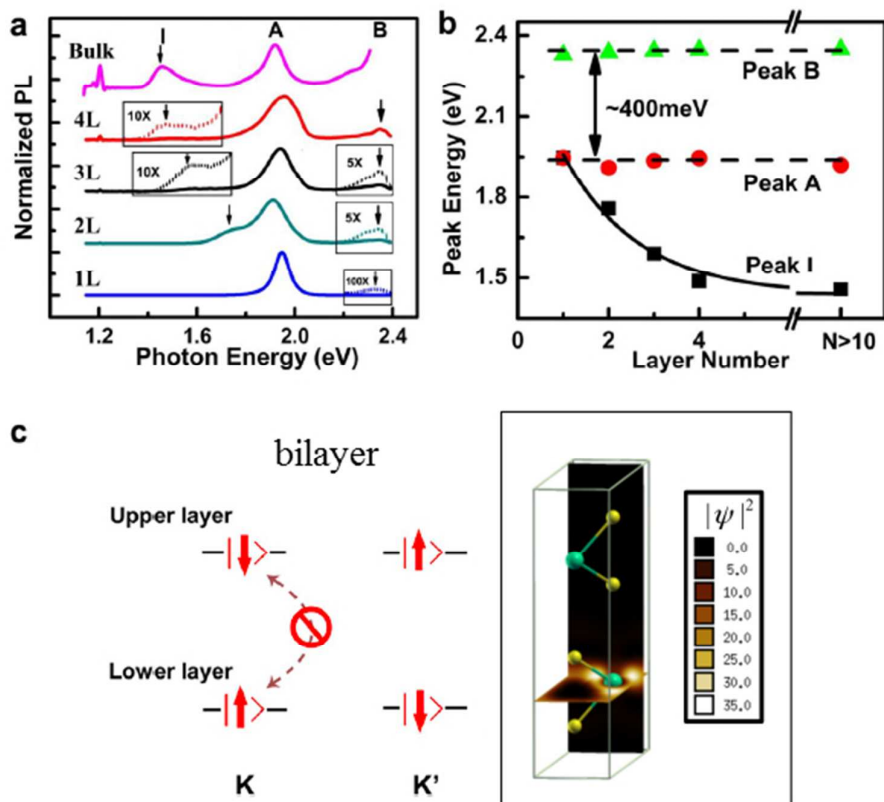


Figure 11. Photoluminescence of bilayer  $\text{WS}_2$  under circularly polarized excitations. (Courtesy of Ref. 28)

(a). Polarization-resolved luminescence spectra with components of  $\sigma_+$  (red) and  $\sigma_-$  (black) under near-resonant  $\sigma_+$  excitation (2.088 eV) at 10 K. Peak A is recognized as the excitonic transition at band edge of direct gap. Peak I originates from the indirect band-gap emission, showing no polarization. Inset presents the circular polarization of the A excitonic transition around the PL peak; (b). The degree of circular polarization as a function of temperature (black). The curve (red) is a fit following a Boltzmann distribution where the intervalley scattering by phonons is assumed; (c). Photoluminescence spectrum of components of  $\sigma_+$  (red) and  $\sigma_-$  (black) under off-resonance  $\sigma_+$  excitation (2.33 eV) at 10 K. A nonzero circular polarization  $P$  is only observed at emissions from A excitons.

